

# Structural Characterization of Particle Systems using Spherical Harmonics

Feinauer, Julian<sup>a,b,\*</sup>, Spettl, Aaron<sup>b</sup>, Manke, Ingo<sup>c</sup>, Strege, Stefan<sup>d</sup>, Kwade, Arno<sup>d</sup>, Pott, Andres<sup>a</sup>, Schmidt, Volker<sup>b</sup>

<sup>a</sup>*Deutsche ACCUmotive GmbH & Co. KG, Kirchheim unter Teck*

<sup>b</sup>*Institute of Stochastics, Ulm University*

<sup>c</sup>*Institute of Applied Materials, Helmholtz-Centre Berlin*

<sup>d</sup>*Institute for Particle Technology, TU Braunschweig*

---

## Abstract

Many important properties of particulate materials are heavily influenced by the size and shape of the constituent particles. Thus, in order to control and improve product quality, it is important to develop a good understanding of the shape and size of the particles that make up a given particulate material. In this paper, we show how the spherical harmonics expansion can be used to approximate particles obtained from tomographic 3D images. This yields an analytic representation of the particles which can be used to calculate structural characteristics. We present an estimation method for the optimal length of expansion depending on individual particle shapes, based on statistical hypothesis testing. A suitable choice of this parameter leads to a smooth approximation that preserves the main shape features of the original particle. To show the wide applicability of this procedure, we use it to approximate particles obtained from two different tomographic 3D datasets of particulate materials. The first one describes an anode material from lithium-ion cells that consists

---

\*Corresponding author

Email address: [julian.feinauer@daimler.com](mailto:julian.feinauer@daimler.com) (Feinauer, Julian)

of sphere-like particles with different sizes. The second dataset describes a powder of highly non-spherical titanium dioxide particles.

*Keywords:* Structural Characterization, Spherical Harmonics, Lithium-Ion Cells, Particle Shape

---

## 1. Introduction

Granular materials are used in many different industrial applications. For instance, they are used as ingredients in pharmaceutical materials and in the production of semiconductors and energy materials such as lithium-ion cells, solar cells and fuel cells [1, 2, 3]. Both the transport and industrial processing of agglomerates are greatly influenced by the shape and size of the agglomerate components [4]. For example, the flow, handling and rheology of granular materials are directly influenced by the shape and size of the constituent particles [1, 5, 6, 7]. The performance of particulate materials also depends directly on their microstructure. For example, the performance of lithium-ion anodes depends strongly on the morphology of graphite particles and their spatial arrangement [8].

Tomographic three dimensional (3D) images are ideal sources for investigation of particle characteristics. Many different imaging techniques exist, including electron tomography [9, 10] and focused ion-beam (FIB) tomography [11, 12], which have resolutions on the nm-scale, synchrotron tomography [13] and X-ray microtomography ( $\mu$ -CT) [14, 15], which have resolutions on the  $\mu$ m-scale, and neutron-tomography [16] which can be used for investigations of larger objects.

Since particles in experimental 3D data sets are represented by sets of voxels, their analysis is a non-trivial task. In addition, particles can

have rough surfaces and there are often artifacts present in the data, e.g., caused by the measurements or preliminary image processing steps like filtering and binarization. Thus, a different particle representation is needed to reproduce the properties of particle shapes, which is suitable for many materials. In some cases, this can be done by using simple geometric objects like spheres, ellipsoids or unions of spheres. However, these simple objects cannot reproduce the shape of more complex particles, because important characteristics like volume, surface area or surface roughness are not preserved.

In this paper, we use the spherical harmonics expansion [17, 18, 19] to calculate an alternative representation of particles based on voxelized objects. Spherical harmonics have proven to be a valuable tool for the representation of particles [20, 21]. The exact shape of a particle is represented as a combination of objects with growing roughness, the spherical harmonic functions. The spherical harmonic functions in the expansion are ordered in a way that the roughness of the functions increases with the length of expansion. This kind of hierarchical representation is essentially influenced by a cutoff parameter to achieve a smooth approximation. The cutoff parameter is crucial as it controls the balance between the quality and the smoothness of the approximation. We present a method for optimally choosing this cutoff parameter,  $L$ , the length of expansion, based on statistical hypothesis testing. We show by comparing the mean square error that in this way an approximation is obtained which is in good accordance with the voxelized representation for complex shaped objects. Furthermore, we use an analytic description of this representation to calculate different particle characteristics and compare them to

those obtained directly from the voxelized objects. A basic characteristic is the radius of an equivalent sphere, where this sphere can be defined to have equal volume, equal surface area or the same minimum or maximum particle axes, depending on the given application [22]. Other characteristics are sphericity [23] and characteristics that are based on the convex hull [24] and Gaussian curvature [25, 26, 27]. We note that the representation of particle shapes in spherical harmonics enables the definition and calculation of more refined characteristics as stated in [28]. Some of these characteristics can be linked with effective physical properties of the materials like diffusive behavior or interfacial reaction rates [8, 29].

In order to demonstrate the potential and generality of this method we apply it to two different particle systems. Both samples are obtained using 3D imaging techniques with subsequent segmentation. The first particle system is extracted from the anode of a lithium-ion cell and consists of  $\text{LiC}_6$  particles. The second sample describes a powder of highly non-spherical  $\text{TiO}_2$  particles.

The rest of this paper is organized as follows. In Section 2, the class of spherical harmonic functions is introduced. We discuss the definition of the boundary for an object which is defined on a voxel grid and present an algorithm for its fast evaluation. For the purpose of implementation, all necessary algorithms and numerical details for the fast and efficient calculation of the coefficients in the spherical harmonics expansion are briefly recalled. Furthermore, we propose a method to estimate the parameter  $L$ , which determines the approximation quality and the smoothing effect in the expansion. In Section 3, this technique is applied to experimental data. After a short description of the materials, the approximation

of particles from both samples by spherical harmonics is described. A comparison of the particle systems from the two different materials is performed using the spherical harmonics expansion. The goodness of approximation is discussed and various structural characteristics like particle sizes, surface areas and surface roughness are calculated. Finally, an outlook to further possibilities regarding the representation of particle systems by means of spherical harmonics concludes the paper.

## 2. Representation of particles by spherical harmonics

In this section we introduce the mathematical background of spherical harmonics and describe the techniques required for application to particles extracted from 3D images. Throughout this section, a particle is taken to be a set of connected voxels in a binary image, where each voxel can only adopt one out of two values which indicates whether the voxel belongs to the foreground or background, respectively. The two possible states are denoted by *true* and *false*. The spherical harmonics are a set of functions defined on the unit sphere which form a basis for a large class of functions. In fact, each square integrable function on the unit sphere can be represented as a series of spherical harmonics. In the situation where the functions define the boundary of the particles, this integrability condition is always naturally fulfilled. An important requirement for the particles is that they are star shaped (or star convex) with respect to a centroid [30], in our case to the barycenter. If this is true, it is possible to define a radius function on the unit sphere to fulfill the conditions for the expansion in spherical harmonic functions. The radius function maps each angle  $(\theta, \phi)$  on the unit sphere to the distance from the cen-

troid to the boundary of the particle in that direction. Star shaped (or star convex) with respect to a point means that the connection from this point to each point of the particle lies completely inside the particle. This means especially that there are no holes or e.g. curved intrusions into the particles. Furthermore, it only makes sense to calculate a smooth approximation of particles if it is reasonable to assume that the observed objects are smooth.

### 2.1. Definition and calculation of the boundary

During the preprocessing of data, the 3D images are binarised and segmented using a morphological segmentation method. In our case, a watershed transform [31, 32, 33, 34] is used. This means that the binary image  $B$  is divided into distinct regions  $B_1, \dots, B_n$  with  $\bigcup_{i=1}^n B_i = B$  and  $B_i \cap B_j = \emptyset$  for  $i \neq j$ . The set of foreground voxels in a region corresponds to exactly one particle. In the following we describe the procedure that is applied to each particle.

The first step is to determine the distance from the barycenter of the particle to the boundary in each direction in order to compute the *radius function*. However, it is not clear how the boundary should be defined to model the original object as accurately as possible. There are several reasons for this. The discretization of the real object, based on grayscale intensities in an image, to Boolean values can be done using some kind of threshold to decide whether a voxel is classified as foreground or background. Thus, it is clear that the boundary cannot be defined without some assumptions about the preliminary step of discretization. Figure 1 shows a 2D example of the consequences of different thresholds for the voxelized object. In the first case, shown in Figure 1(a), every voxel that

covers a part of the original object, which means that it has an intensity value larger than zero, is put to foreground which leads to an overestimation of the size of the object. In the other case, considered in Figure 1(b), only voxels that are completely inside the object, which means that their intensity has the maximal value, are marked as foreground which leads to an underestimation of the size of the object.

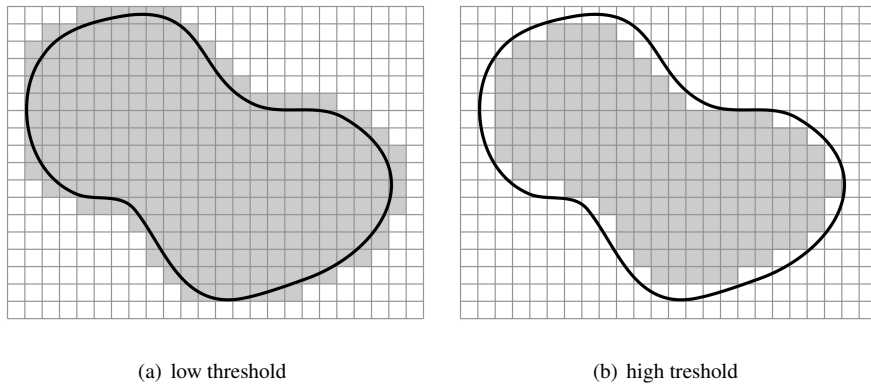


Figure 1: Schematic illustration of the effect of a low or a high threshold for the shape of the object in the binary image.

Therefore, it is important to have information on the choice of the threshold and other preliminary steps for the binarization. In the extreme cases discussed above one can perform a morphological erosion or dilation [35] as a correction.

After a suitable preprocessing of the particle, we need to determine the exact distance from the centroid to the boundary for each direction on the unit sphere. As stated above, we assume that the particle is star shaped to ensure that the algorithm proposed below yields valid results in all cases. For a given angle,  $(\theta, \phi)$ , we use nested intervals for an efficient evaluation of the particle boundary of the voxelized particles. We use the diagonal size,  $d$ , of the bounding box calculated for the original object as

an upper bound for the radius in each direction. We then consider the following procedure:

- (1) Construct a unit vector  $e$  in direction  $(\theta, \phi)$ .
- (2) Put the initial interval  $[a, b] = [0, d]$ .
- (3) If  $(a+b)/2 \cdot e$  belongs to the particle, then put  $a = (a+b)/2$ , otherwise set  $b = (a+b)/2$ .
- (4) Repeat step 3 if  $b - a > \tau$ , where  $\tau$  is some required (maximum) tolerance.
- (5) The result is  $r(\theta, \phi) = (a + b)/2$ .

A schematic illustration of this procedure is shown in Figure 2. The advantage of nested intervals is that the runtime of the algorithm is, in practice, nearly independent of the particle size because the computational effort is logarithmic in the diameter of the particle's bounding box for a fixed tolerance. The boundary in direction  $(\theta, \phi)$  can then be represented in Cartesian coordinates relative to the centroid by

$$\begin{aligned} x &= r(\theta, \phi) \sin \theta \cos \phi, \\ y &= r(\theta, \phi) \sin \theta \sin \phi, \\ z &= r(\theta, \phi) \cos \theta. \end{aligned} \tag{2.1}$$

## 2.2. Expansion in spherical harmonics

The set of spherical harmonic functions  $\{Y_l^m : [0, \pi] \times [0, 2\pi) \rightarrow [0, \infty) : l, m \geq 0\}$  is a basis for the family of square integrable functions defined on the unit sphere. This means that the radius function for

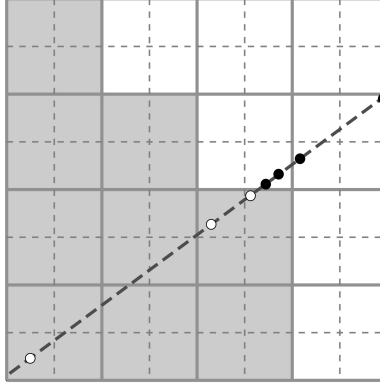


Figure 2: Schematic description of nested intervals with lower boundaries as white points and upper boundaries as black points. The small dashed lines in gray display the integer points in the grid and the black dashed line displays the search direction.

a given particle can be expanded in terms of spherical harmonics, if the particle is star shaped. The spherical harmonics  $Y_l^m$  are organized in a special way. The subscript  $l$  denotes the degree and the superscript  $m$  is called the order. An application to single particles has been shown in [36].

In the following, we describe an efficient way to calculate the coefficients of the expansion with respect to the spherical harmonics for a large set of particles. In our setup, we deal with a function  $r : [0, \pi] \times [0, 2\pi] \rightarrow [0, \infty)$ . The expansion in spherical harmonics is then given by

$$r(\theta, \phi) = \sum_{l=0}^{\infty} \sum_{m=-l}^l c_l^m Y_l^m(\theta, \phi), \quad (2.2)$$

where the coefficients  $c_l^m$  are called the *spherical harmonics coefficients* of the radius function  $r$  of the underlying particle, and for any pair of integers  $l, m \geq 0$  with  $-l \leq m \leq l$  the spherical harmonic function  $Y_l^m$

is given by

$$Y_l^m(\theta, \phi) = (\sin \theta)^m P_{l-m}^{(m,m)}(\cos \theta) \frac{e^{im\phi}}{\sqrt{2\pi}}. \quad (2.3)$$

Here,  $P_{l-m}^{(m,m)}$  denotes a *Jacobi polynomial*, which can be calculated efficiently using the following recursion formula [19]:

$$\begin{aligned} P_k^{(m,m)}(x) = & 2xP_{k-1}^{(m,m)}(x) \left(1 + \frac{m-1/2}{k}\right)^{1/2} \left(1 - \frac{m-1/2}{k+2m}\right)^{1/2} \\ & - P_{k-2}^{(m,m)}(x) \left(1 + \frac{4}{2k+2m-3}\right)^{1/2} \\ & \left(1 - \frac{1}{k}\right)^{1/2} \left(1 - \frac{1}{k+2m}\right)^{1/2}, \end{aligned} \quad (2.4)$$

with

$$\begin{aligned} P_{-1}^{(m,m)}(x) & \equiv 0, \\ P_0^{(m,m)}(x) & \equiv \frac{1}{\sqrt{2}} \prod_{j=1}^m \sqrt{1 + \frac{1}{2j}}. \end{aligned} \quad (2.5)$$

The calculation of the spherical harmonics coefficients of a radius function  $r$  is then done using the relation

$$c_l^m = \int_0^{2\pi} \int_0^\pi r(\theta, \phi) Y_l^{m*}(\theta, \phi) \sin \theta \, d\theta \, d\phi, \quad (2.6)$$

where  $*$  denotes the complex conjugate. For the numerical evaluation of the coefficients  $c_l^m$  we use an equiangular grid  $G$  on the sphere with  $N$  supporting points for each component:

$$G = \left\{ (\theta_i, \phi_j) = \left( \pi \frac{i+1/2}{N}, 2\pi \frac{j}{N} \right) : i, j \in \mathbb{Z}, 0 \leq i, j, < N \right\}. \quad (2.7)$$

For more details on this choice of grid see [19]. Using (2.3) and changing the order of integration, the double integral in (2.6) can be interpreted as a Fourier transform and an integral over the associated Legendre polynomial, i.e.,

$$c_l^m = \int_0^\pi \left( \int_0^{2\pi} r(\theta, \phi) \frac{e^{-im\phi}}{\sqrt{2\pi}} \, d\phi \right) (\sin \theta)^m \tilde{P}_{n-m}^{(m,m)}(\cos \theta) \sin \theta \, d\theta.$$

The discretized version of the inner integral using the grid  $G$  can be calculated using the fast Fourier transform [37] and for the outer integral a suitable set of integration weights is given by

$$w_N(i) = \frac{2\sqrt{2}}{N} \sum_{k=0}^{N/2-1} \frac{1}{2k+1} \sin((2l+1)\theta_i), \quad (2.8)$$

where  $N$  denotes the number of supporting points and  $\theta_i$  is given by the grid in (2.7), see [38] and [19]. For further details on the theory of spherical harmonics, see e.g. [17, 18].

As mentioned above, the representation in spherical harmonics is hierarchical in the sense that spherical harmonic functions with a smaller degree describe coarser shapes and the shapes become finer with higher degrees. Thus, we can control the quality of approximation by limiting the number of coefficients in the expansion. This step determines the quality of the approximation, as a longer series leads to a more accurate reproduction of the original object. A short series, on the other hand, has a smoothing effect where sharp edges and small artifacts from the imaging or postprocessing can be avoided in the approximated particle. This is similar to limiting the “bandwidth”, something that is used often by engineers when dealing with noisy data [39]. In our situation this means that the series is truncated after a maximum degree  $L$ , which leads to the limited expansion

$$r_L(\theta, \phi) = \sum_{l=0}^L \sum_{m=-l}^l c_l^m Y_l^m(\theta, \phi), \quad (2.9)$$

with the same coefficients as in (2.2).

### 2.3. Estimation of the maximum degree $L$

The parameter  $L$  that describes the length of expansion in (2.9) is crucial and has a large effect on the calculation of structural characteristics. If  $L$  is chosen too small, then important features of the particle shape are neglected. If  $L$  is chosen too large the smoothing effect is lost. A comparison of approximations of a particle from the first dataset presented in Section 3.1 for different values of  $L$  is shown in Figure 3.

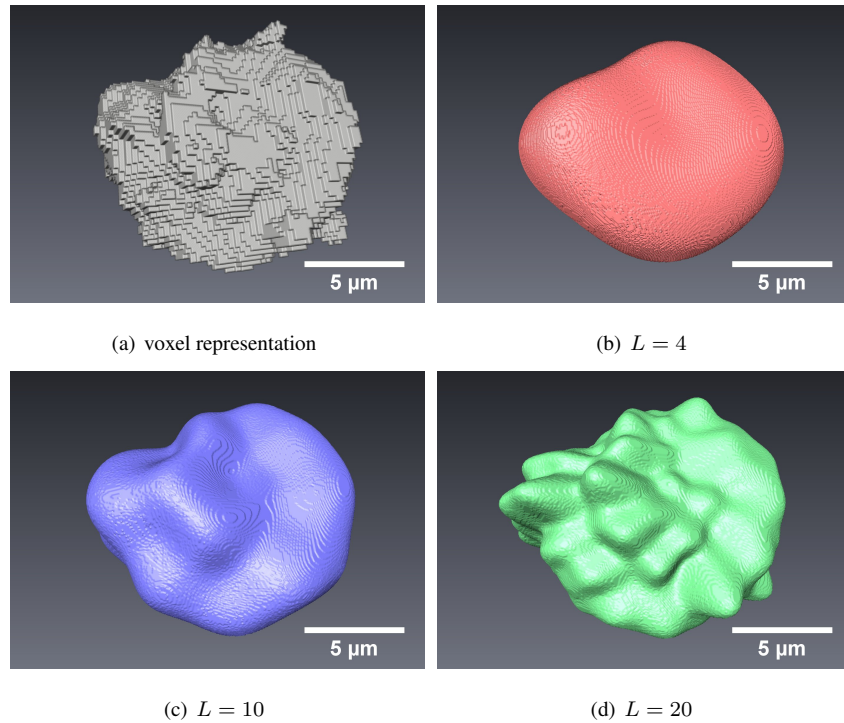


Figure 3: Rendering of a single particle from a lithium-ion cell anode and spherical harmonic approximations with different lengths of expansions.

In order to determine an optimal value of  $L$  we do not compare the particle and the approximation directly. Although, to illustrate the influence of the representation on different characteristics we do show the values calculated for both representations. This is due to the fact that a

direct comparison like computing the  $\mathcal{L}^2$ -norm would always favor an exact representation which is counterproductive to the smoothing aspect. Instead, we use a stochastic approach to evaluate the accordance of a particle and its approximation. It is important to note that this procedure makes only sense if it is reasonable to assume that the particles observed in the experimental data have smooth surfaces. We draw  $S \gg 1$  points from a uniform distribution on the unit sphere using the method described in [40] and compute the radius of the original particle as well as the approximation with respect to these  $S$  uniformly distributed directions. Note that the choice of  $S$  is motivated in Section 3.2, where we obtained a suitable value of  $S=100$  for our datasets. The set of observations from the original particle is then compared to the set with the values from the approximated particle. We perform a Kolmogorov-Smirnov test [41, 42] with the null hypothesis  $H_0 : F_1 = F_2$ , where  $F_1$  denotes the distribution of the radial values of the original particle and  $F_2$  the distribution of the radial values of the approximated particle.

The Kolmogorov-Smirnov test is performed for each particle in the sample for different values of  $L$  a 100 times where a 5% significance level is used. It is important to note that the Kolmogorov-Smirnov test is designed for independent samples and the samples in our case are not completely independent. But as the random points on the unit sphere are in most cases not too near to each other the application of the Kolmogorov-Smirnov test seems to be reasonable. Thus, we calculate the rejection rate and choose the smallest value of  $L$  which leads to a rejection rate smaller than 5%. This technique works appropriately in practice, cf. Section 3.1. For a more or less detailed approximation the rejection rate

threshold can be varied.

### 3. Application to experimental 3D image data

In this section we explain how the description of particles by spherical harmonics can be used to approximate and characterize particles extracted from 3D image data. To demonstrate the generality of this approach, we consider two datasets describing particle systems of different nature. One shows sphere-like particles in a lithium-ion cell anode. The other one shows a powder of apparently randomly shaped  $\text{TiO}_2$  particles. Cross-sections of both samples are shown in Figure 4.

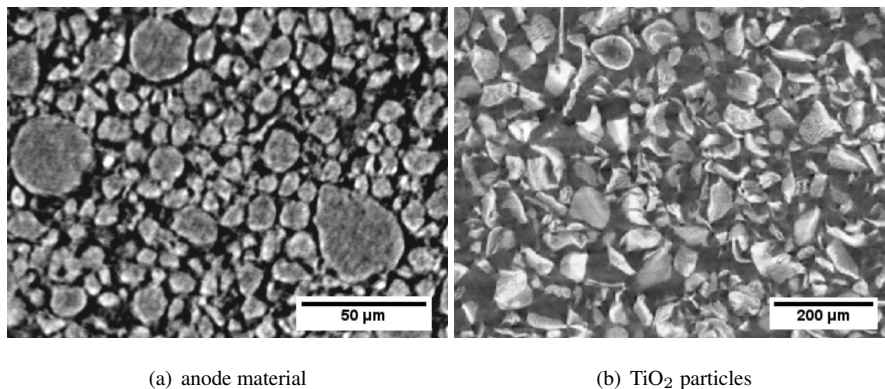


Figure 4: 2D cross-sections of 3D grayscale images.

#### 3.1. Description of experimental image data

The first sample (sample I) is a cutout of an anode from a lithium-ion battery investigated with synchrotron tomography. The anode consists of a system of connected graphite ( $\text{LiC}_6$ ) particles. For more details on the production of anodes for lithium ion cells we refer to [43, 44, 45, 46]. The measurements were performed at the electron storage ring BESSY (Helmholtz Centre Berlin, BAMline). An optical set-up (Optique

Peter) and a 20  $\mu\text{m}$ -thick CWO scintillator screen were used to detect the X-rays. An X-ray energy of 15 keV was chosen. Overall 2200 single radiographic projections were taken for 3D data reconstruction. From a first impression most particles could be described as sphere-like and regular.

The second dataset (sample II) describes a powder of irregular shaped  $\text{TiO}_2$  aggregates, i.e. particles which are composed of many very small primary particles. For imaging purposes the powder has been filled into a thin-walled glass capillary with an inner diameter 2 mm and wall thickness of about 50  $\mu\text{m}$ . The image was then obtained by a high resolution XMT device (MicroXCT 400, Xradia, Inc., USA) [47]. In order to prepare well-defined specimens, a powder tester has been developed and integrated into the XMT system [15, 47]. For 3D imaging of sample II an X-ray energy of 50 keV was chosen. From 3000 single radiograph projections a  $2k^3$  Dataset with a spatial resolution of 1.1  $\mu\text{m}/\text{voxel}$  was reconstructed. For a convenient post processing the dataset was then resampled to  $1k^3$  resulting in a resolution of 2.2  $\mu\text{m}/\text{voxel}$ . From a first inspection it is clearly visible that the particles have irregular shapes and sharp edges.

To extract more detailed information about the particles, a 3D watershed algorithm has been applied [31, 32, 33, 34] to both samples after binarization. More precisely, we employed a stochastic watershed technique to reduce oversegmentation, see [48].

The voxel size for sample I is 0.44  $\mu\text{m}$  in each direction. The cutout has a size of  $1909 \times 1785 \times 116$  voxels. The volume fraction of the particle system is 72.8% and the watershed segmentation identifies 61280 differ-

ent particles. For sample II the voxel size is  $2.2\ \mu\text{m}$  in each direction and the 3D image has a size of  $1972 \times 2014 \times 2014$  voxels. The volume fraction of the particles is 54% and the segmentation identifies 20905 particles. A comparison of the radii of volume equivalent spheres shows that the particles from the lithium-ion anode are smaller—measured in voxels, because this is the relevant scale for the methodology. The mean radius of the volume equivalent spheres for the anode particles is 7.67 voxels with standard deviation of 4.09 voxels. For the particles from the  $\text{TiO}_2$  powder the mean value is 12.67 voxels with standard deviation of 5.56 voxels. Note that the real size of particles is not important for our approximation technique, but their size with respect to the voxel grid is, of course.

### 3.2. *Selecting the number of points $S$*

Obviously, the choice of the number of directions  $S$  that are considered in the algorithm for determining an optimal  $L$  (see Section 2.3) plays a huge role. Thus, we performed some tests to find a relation between the noise one expects in the image and suitable values for  $S$ .

This is done as follows. For both materials considered here 500 particles have been chosen randomly and approximated by spherical harmonics with  $L = 5$ . These are called test particles in the following. All test particles have been superimposed with two different modes of noise. The optimal length of expansion is estimated for the noisy particles and different values of  $S$ . The approximations are then compared to the "ground truth" before the addition of noise.

For the comparison, three different error types are considered. First, we look at the relative  $\mathcal{L}^2$ -norm (with respect to the  $\mathcal{L}^2$ -norm of the

"ground truth"). Furthermore, we look at the symmetric difference between both representations of the particles. For two sets  $A$  and  $B$ , we define the relative symmetric difference volume as the ratio between the volumes of the symmetric difference  $A\Delta B$  and the volume of their union  $A\cup B$ . Finally, we also consider the Hausdorff distance between both particles which is given by  $d_H(A, B) = \max \{ \sup_{x \in A} d(x, B), \sup_{y \in B} d(y, A) \}$  for two (non-empty) sets  $A$  and  $B$ , where  $d(x, A) = \inf_{a \in A} d(x, a)$  denotes the minimal distance from an arbitrary point  $x$  to the set  $A$ . For more details, we refer to [49].

To mimic the uncertainty in boundaries of particles in tomographic images, which could be caused by variations in material densities or originate from artifacts of the measurements, we consider a roughening of surfaces as noise. The algorithm to obtain a noisy particle is as follows.

1. Plot the test particle, i.e., discretize on voxel grid.
2. For each surface voxel perform an Bernoulli experiment with parameter  $p = 0.01$ . If the experiment is successful (with probability  $p$ ), perform Step 3, otherwise skip the voxel.
3. A ball is placed around the voxel with radius  $r = \sqrt{2}$ . Perform another Bernoulli experiment with  $p = 0.5$  to determine if the ball is added to or subtracted from the voxelized particle representation.

An important requirement for the expansion in spherical harmonics is, as stated above, that the particles are star-shaped. Thus, the simulated noise should not alter this property of the particles. With the algorithm stated above it is not clear that star-shaped particles keep this property after the addition of noise. But, a rough surface in tomographic data is

only approximately star-shaped, too. An example of a noisy test particle is shown in Figure 5. The results of the approximation error can be seen in Figure 6. As expected, the approximation error decreases for higher values for  $S$  for all types of errors considered here. This is due to the fact that a higher number of observations  $S$  leads to a more precise representation of particles.

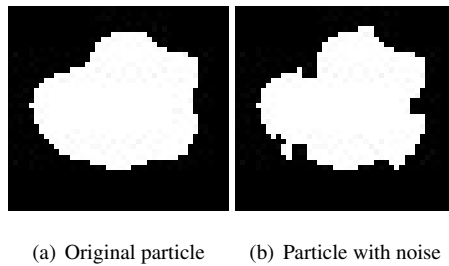


Figure 5: 2D cross-section of a particle without and with simulated surface roughness.

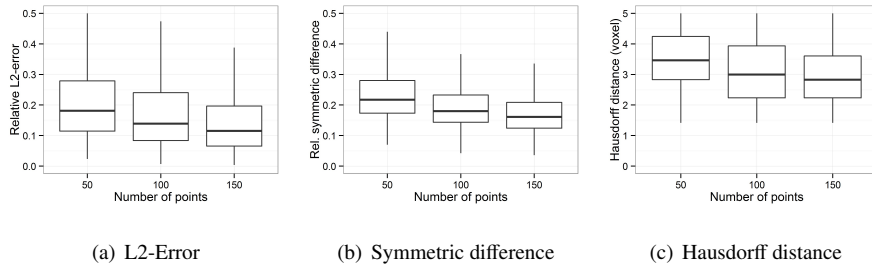
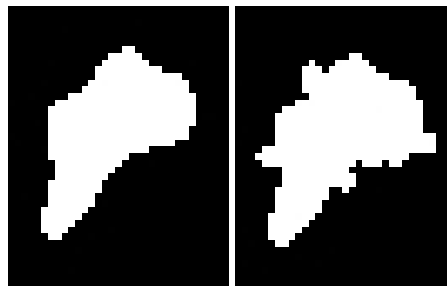


Figure 6: Boxplots of three different error types for 1000 particles with noise.

Another type of noise considered are spikes emanating from the particles surfaces, which can be observed in experimental data. In the exemplary particle from a lithium-ion cell shown in Figure 3(a) one can see multiple spikes above the particle or on the right-hand side. As the particles have been processed in an high energy disperser it is unlikely that these spikes belong to the particles. Thus, we take these artifacts into consideration. To mimic this effect we use the following method:

1. Plot the test particle, i.e., discretize on voxel grid.
2. For each surface voxel, perform an Bernoulli experiment with probability  $p = 0.01$ . If the experiment is successful perform Step 3, otherwise skip the voxel.
3. A tube is drawn from the voxel in direction of the connecting line from the barycenter of the test particle to the boundary voxel. The length of the tube is set to 3.0 and the diameter is set to 3.0.

From this method it is clear that the particles with noise are still star-shaped and our method can be applied straightforward. A particle with simulated spikes is shown in Figure 7. The calculated errors are shown in Figure 8. As one can see, the tendency is contrary to the one in Figure 6. A higher number of observation points  $S$  leads to a larger error, which can be explained by the fact that small spikes are "ignored" for small values of  $S$  as no (or only few) observations are subject to the error induced by the spike.



(a) Original particle      (b) Particle with noise

Figure 7: 2D cross-section of an particle with and without spikes.

Overall, one can see, that a smaller value of  $S$  around 50 minimizes the error when spikes are present in the particles. If the particles have

rough surfaces then a higher value of  $S$  around 150 is favorable. Thus, we choose  $S = 100$  as trade off in our situation. Note that the absolute values for two of the three error measures are approximately equal at  $S = 100$ .

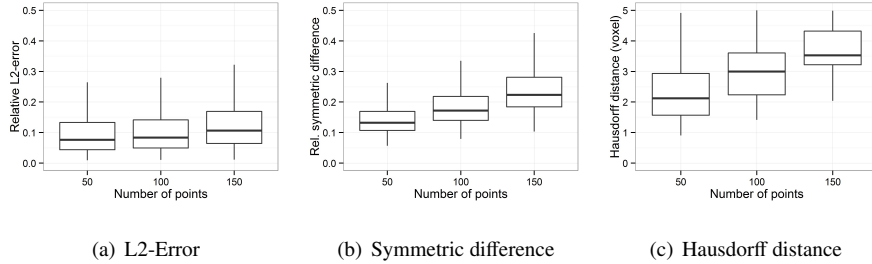


Figure 8: Boxplots of three different error types for 1000 particles with spikes.

### 3.3. Particle approximation

The particles from both materials are approximated by spherical harmonics. The particles of the anode material appear to be very sphere-like and therefore one could expect a good accordance even with a small number of coefficients. The particles from the powder material are much more irregular and apparently not even always convex but it turns out that the particles are still star shaped.

To speed up the calculations we precompute the associated Legendre polynomials given in (2.4) and (2.5) as well as the numeric weights given in (2.8) and use them for all particles. The coefficients are then calculated using the numerical method described in Section 2.3 with  $N = 256$  in (2.7). For both sets of particles we estimate the value of  $L$  for the expansion of every particle, see Figure 9. For sample I (anode material) we get the mean value  $\mu_L^I = 4.60$  and for sample II ( $\text{TiO}_2$  particles) we get the value  $\mu_L^{II} = 4.36$ . In Figure 10 we show a boxplot of the radii

$r$  of volume equivalent spheres over the length of expansion  $L$  for both materials. One can see that the size of the particles has a slight influence on the length of expansion for the lithium-ion cell anode sample. For the particles from the  $\text{TiO}_2$  there is no significant trend. The decreasing mean radius for larger values of  $L$  in the anode material can be explained by the fact that a portion of the small particles in this material was generated by larger particles breaking apart. This means that those particles have a higher tendency to sharp edges, which leads to longer expansions.

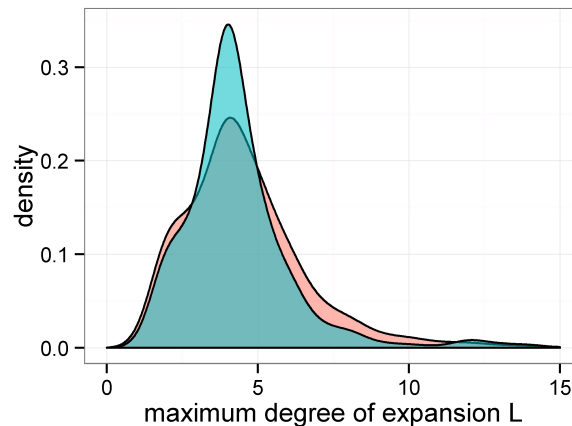


Figure 9: Distribution of the  $L$  values chosen individually for every particle: anode material (red) and  $\text{TiO}_2$  particles (blue)

A 3D rendering of voxelized and approximated particles from the anode material is shown in Figure 11.

#### 3.4. Comparison of both datasets

In this section, we look at different structural properties of particles from both materials and compare them to each other. This includes the approximation error, as well as structural characteristics like the specific

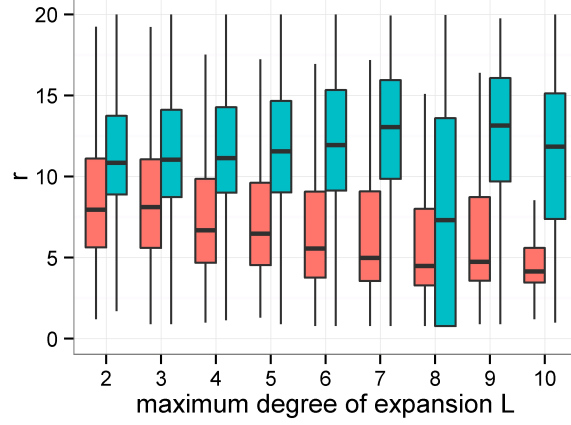


Figure 10: Boxplot of the radii of volume equivalent spheres over the length of expansion  $L$  for both types of particles: anode material (red) and  $\text{TiO}_2$  particles (blue)

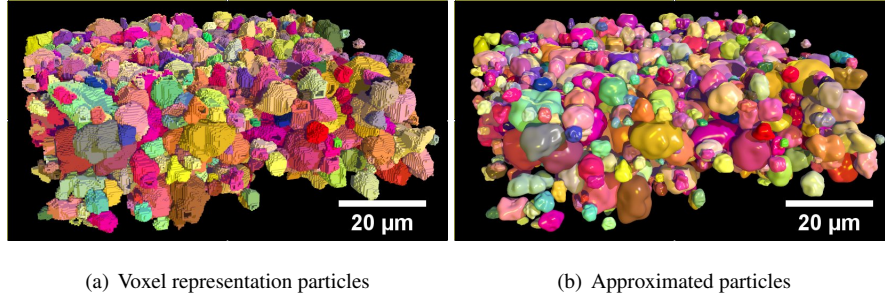


Figure 11: 3D rendering of voxelized and approximated particles for the system of densely packed particles from the anode material.

surface area, the sphericity and the integral of the absolute curvature as a measure for surface roughness.

For a formal examination of the approximation quality, we use the root of the normalized mean squared error, i.e.,

$$E_{\text{particle}} = \sqrt{\frac{\int_0^{2\pi} \int_0^\pi (r(\theta, \phi) - r_L(\theta, \phi))^2 \sin \theta \, d\theta d\phi}{\int_0^{2\pi} \int_0^\pi r^2(\theta, \phi) \sin \theta \, d\theta d\phi}}.$$

The normalization is necessary to compare particles with different sizes. In Figure 12 we plot the frequencies of the approximation errors for all

particles. Note that Figure 12 shows the estimated density function of the approximation error evaluated for all particles. The difference to a histogram is that the observations are not only counted in a fixed interval, but each point of the axis is assigned a value depending on the number of points in its neighborhood and their distance. More precisely, we use a kernel density estimation with Gaussian kernel and bandwidth  $h = 0.01$ , see [50, 51] for details. From Figure 12 it can be seen that, as expected, sphere-like particles from the battery anode can be described better by spherical harmonics than the  $\text{TiO}_2$  particles. The mean approximation error for sample I is  $\mu_E^I = 0.10$  with standard deviation  $\sigma_E^I = 0.038$ , whereas we have  $\mu_E^{II} = 0.15$  with standard deviation  $\sigma_E^{II} = 0.057$  for sample II. Both, mean value and standard deviation are higher for the  $\text{TiO}_2$  material (sample II). This is due to the more irregular shapes of the particles in sample II.

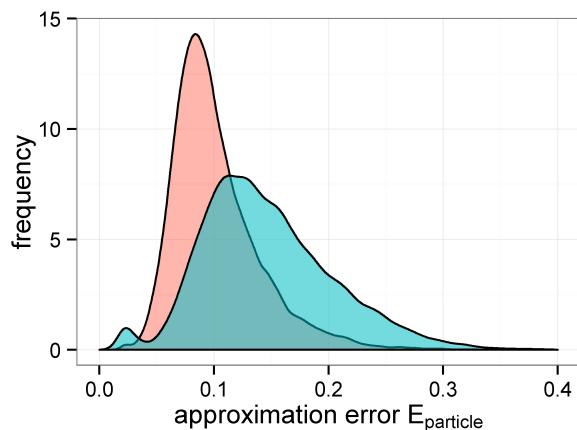


Figure 12: Comparison of the particle approximation error  $E_{\text{particle}}$ : anode material (red),  $\text{TiO}_2$  particles (blue)

### 3.4.1. Volume

The calculation of structural characteristics is an important task in the analysis of 3D image data. First, we look at the particle volumes, calculated by

$$V_{\text{particle}} = \frac{1}{3} \int_0^\pi \int_0^{2\pi} r_L^3(\theta, \phi) \sin \theta \, d\phi d\theta.$$

This equation can be evaluated easily if the coefficients of the expansion are known and it is easy to implement. However, there exist methods to calculate the volume of a given approximation faster using formulas based on the convolution of coefficients, see [52].

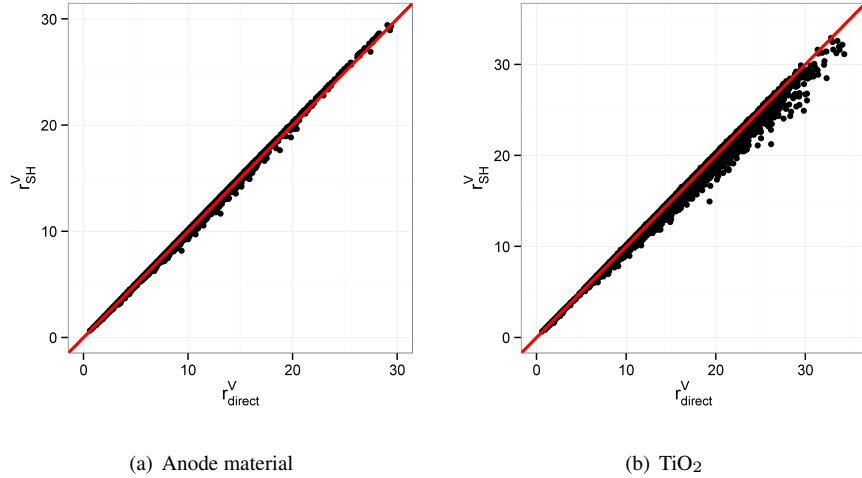


Figure 13: Visualization of the radii of volume-equivalent balls; calculated by spherical harmonics and by direct estimation from voxelized data. Each dot represents a particle from the respective material.

Figure 13 shows a comparison of the radii  $r_{\text{SH}}^V$  and  $r_{\text{direct}}^V$  of volume-equivalent balls calculated based on the volumes obtained from the spherical harmonics approximation and the volumes computed directly from voxelated data. It can be seen that these radii are very similar for both samples, but not identical. For the particles from the anode material the

accordance is slightly better than for the TiO<sub>2</sub> particles. And, in addition, the TiO<sub>2</sub> particles are approximated with a smaller  $L$  value and have a more irregular shape.

### 3.4.2. Surface area

Another important characteristic of particles is their (specific) surface area. First, we compare surface areas obtained using spherical harmonics, which can be calculated by

$$S_{\text{particle}} = \int_0^\pi \int_0^{2\pi} r_L(\theta, \phi) \left( \left( \frac{\partial}{\partial \phi} r_L(\theta, \phi) \right)^2 + \left( \frac{\partial}{\partial \theta} r_L(\theta, \phi) \right)^2 \sin^2 \theta + r_L^2(\theta, \phi) \sin^2 \theta \right)^{1/2} d\phi d\theta, \quad (3.1)$$

to a surface area estimation based on weighted local voxel configurations [53]. The idea of this approach is that one can reconstruct an approximation for the "real shape" of an underlying object based on  $2 \times 2 \times 2$  voxel squares. For each possible configuration one can thus calculate the surface area one would expect based on the voxel representation. These surface areas are the weights for the local  $2 \times 2 \times 2$  voxel configurations. See Figure 14 for a comparison of the radii  $r_{\text{SH}}^S$  and  $r_{\text{LW}}^S$  of surface area-equivalent balls for the surface calculated by spherical harmonics and local weights respectively. It turns out that spherical harmonics tend to give us smaller estimates, which makes sense as they generate smoother surfaces, and we aim to neglect effects caused by discretization or noise. Clearly, this effect is more noticeable for larger particles. Again this tendency is more visible for the TiO<sub>2</sub> particles due to their larger surfaces and irregular shapes.

Note that in (3.1) all expressions can be evaluated very fast for spherical harmonics. The derivatives with respect to  $\theta$  and  $\phi$  can be calculated from (2.3) and (2.9). The calculation of the surface area using (3.1) is computationally expensive. Due to the square root in the expression there exists no fast formula for the calculation of the surface area. However, we would like to note that there exist formulas for a fast and efficient calculation of lower and upper bounds for the surface area that may be sufficient in some applications, see [52] for more details.

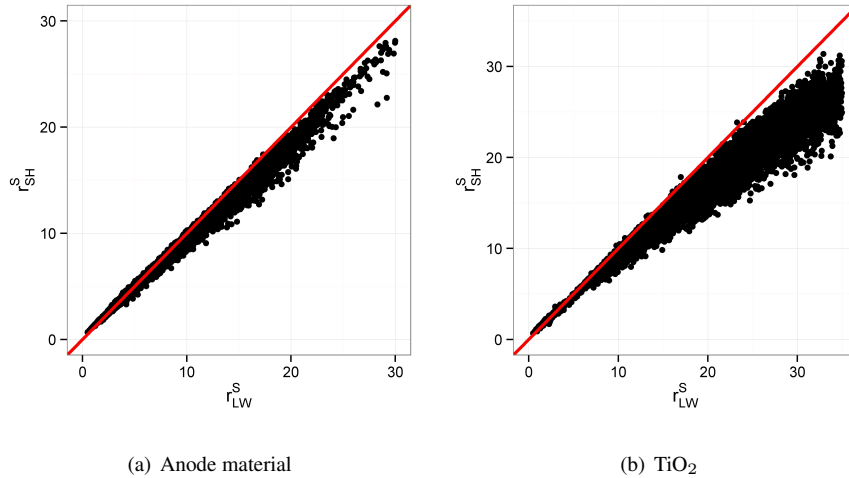


Figure 14: Visualization of the radii of surface-equivalent balls; surface area calculated by spherical harmonics and by local weights directly from voxelized data. Each dot represents a particle from the respective material.

Furthermore, we consider the specific surface area, i.e., the surface area of an object divided by its volume. This is important for active materials used in anodes of lithium-ion cells to characterize the balance between energy storage and charging / discharging behavior due to intercalation at the surface, where the specific surface area for a particle is

defined by

$$\text{SSA}_{\text{particle}} = \frac{S_{\text{particle}}}{V_{\text{particle}}}.$$

For the two materials discussed in this paper, the specific surface area of particles is shown in Figure 15. In Figure 15(a) it looks as if the particles from the anode material have a larger specific surface area which is not intuitive, since the shapes of the  $\text{TiO}_2$  particles seem to be more irregular. This is due to the varying sizes of the particles. For a ball the SSA can be expressed explicitly as  $3/r$ . Therefore, the normalized specific surface area  $\text{SSA}_{\text{norm}} = \frac{\text{SSA} \cdot r}{3}$ , with  $r$  calculated from the sphere with equal volume is shown in Figure 15(b). As expected, the normalized specific surface area which corresponds to a surface based shape factor is clearly larger for irregular ( $\text{TiO}_2$ ) particles. For the  $\text{TiO}_2$  particles the distribution is wider. This is in good agreement with what one would expect from the optical inspection of both samples, because the particles from the anode sample look more spherical than those from sample II.

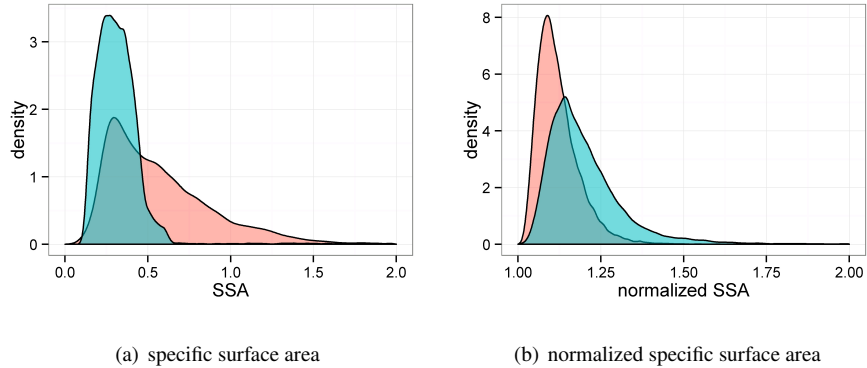


Figure 15: Specific surface area (SSA) of particles directly calculated and with normalization: anode material (red),  $\text{TiO}_2$  particles (blue)

### 3.4.3. Sphericity

A further characteristic which is frequently considered in various applications is the sphericity of particles  $\Psi$ . There exist different definitions of this characteristic in the literature, we however define it as the ratio of the surface area of the volume-equivalent ball divided by the surface area of the corresponding particle, i.e.,

$$\Psi_{\text{particle}} = \frac{\pi^{1/3}(6V_{\text{particle}})^{2/3}}{S_{\text{particle}}},$$

see [54]. Figure 16 shows the estimated sphericities of particles, with volume and surface obtained from voxelized data and with volume and surface calculated using spherical harmonics, respectively. As expected, the particles from the anode material show a higher sphericity in both cases. Sphericities estimated using spherical harmonics are larger for both materials, because the surface of particles is smoothed, which leads to a smaller surface area as shown in Figure 14 and discussed above. The comparison of the sphericities which have been calculated by the methods considered in Figures 16(a) and 16(b) shows that there are quite significant differences. We suppose that these differences are caused by the imprecise estimation of surface area, especially for small and irregularly shaped objects.

### 3.4.4. Surface roughness

For a more detailed characterization of particle surfaces we look at the surface roughness, which we define as

$$R = \int_0^\pi \int_0^{2\pi} |K(\theta, \phi)| \, d\phi d\theta,$$

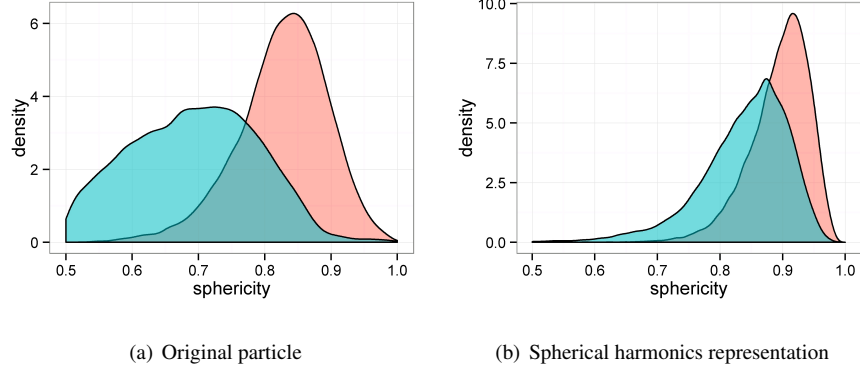


Figure 16: Sphericity calculated from the original particle and the spherical harmonics representation: anode material (red), TiO<sub>2</sub> particles (blue)

where  $K(\theta, \phi)$  denotes the Gaussian curvature at the surface point in direction  $(\theta, \phi)$  which is given by

$$K(\theta, \phi) = \frac{-X_\theta \cdot n_\theta X_\phi \cdot n_\phi + \frac{1}{2}(X_\theta \cdot n_\phi + X_\phi \cdot n_\theta)}{r_\theta^2(r_\phi^2 + r^2 \sin^2 \theta) - r_\theta^2 r^2}, \quad (3.2)$$

with

$$X(\theta, \phi) = \begin{pmatrix} x(\theta, \phi) \\ y(\theta, \phi) \\ z(\theta, \phi) \end{pmatrix}$$

where  $x$ ,  $y$  and  $z$  are defined in (2.1). In addition,  $n$  denotes the unit normal vector, which can be calculated using

$$n = \frac{X_\theta \times X_\phi}{|X_\theta \times X_\phi|}.$$

The subscripts in (3.2) denote derivatives in the respective directions. The idea of this quantity for roughness is that the Gaussian curvature has large values where the curvature of the surface changes. This means that a blistered surface will lead to a large value for the integrated absolute curvature. For a comparison we show the estimated values for

this characteristic for the particles of both datasets in Figure 17. In Figure 17(a) the calculated values are visualized which have been obtained using the spherical harmonics approximation of the particles. It is important to note that such characteristics that involve second order derivatives along the particle surface cannot be evaluated directly from the voxelized particles. However, the value of the curvature is not only influenced by the shape of the particle, but also by the size of the particles, as the roughness for a sphere with radius  $r$  is  $4\pi/r^2$ . Therefore, we also look at the normalized roughness  $R_{\text{norm}} = r^2 R / (4\pi)$  where  $r$  is the radius of the volume-equivalent ball. The results obtained for this quantity are shown in Figure 17(b).

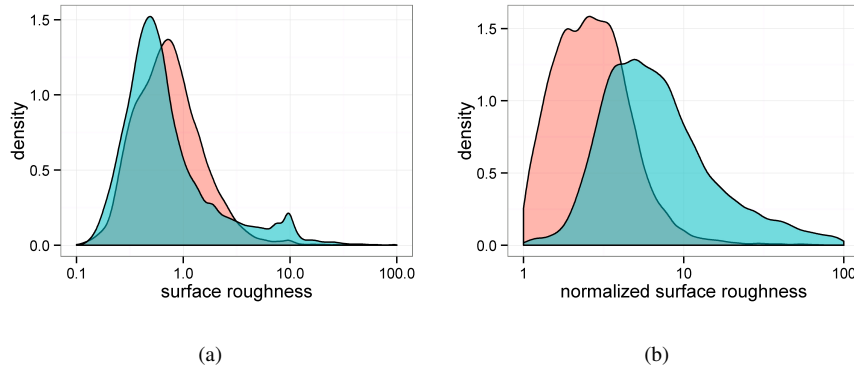


Figure 17: Roughness of particles on logarithmic scale calculated for spherical harmonic approximation: anode material (red),  $\text{TiO}_2$  particles (blue)

#### 4. Conclusions and outlook

In this paper we have shown how an analytical description of particles can be obtained using an expansion in terms of spherical harmonics. We discuss the problem of discretization present in voxelized (experimental

and noisy) data. Using our approach, this problem can be treated elegantly by determining the length of expansion using a statistical testing approach, which leads to a proper and smooth representation of particles. An analytical description of particles has several advantages. First, it can be used directly for modeling, where mostly simple objects like spheres have been used so far in the literature. Second, an analytical description allows the application of standard formulae for the calculation of structural characteristics like surface area and other shape-related quantities. The surface of each particle is given by a smooth function and derivatives can be obtained easily, which is always a problem for voxelized data. To demonstrate the potential and generality of our method, we have applied it to two different particle systems. The first particle system is extracted from the anode of a lithium-ion cell. The second material sample is a powder of highly non-spherical  $\text{TiO}_2$  particles. The particles from both samples are approximated by spherical harmonics, and important structural characteristics are calculated and compared.

Depending on the kind of application, it may be useful to split the particle description into size, shape and rotation. Therefore, it should be noted that, for spherical harmonics as described in this paper, the description of shape is not rotation-invariant, which means that the description of a given object will change when the object is rotated. We refer to [55], where rotation invariant descriptors are presented that are based on spherical harmonics.

In a forthcoming paper, we will use the expansion in terms of spherical harmonics for stochastic modeling of particulate materials with densely packed particles, e.g., battery electrodes. As explained in the introduc-

tion, this will allow us to match important structural characteristics observed in experimental data, e.g., surface areas. The flexibility provided by the spherical harmonics is central for this approach.

### Acknowledgments

This work was partially funded by DFG under grant number 997/14-1 in the priority programme 1679 “Dynamische Simulation vernetzter Feststoffprozesse” and under grant number 9/11-2 in the priority programme 1486 “Partikel im Kontakt” as well as by BMBF under grant number 05M13VUA in the programme “Mathematik für Innovationen in Industrie und Dienstleistungen”. We are grateful to Tim Brereton for a critical reading of the manuscript.

- [1] H. Bockholt, W. Haselrieder, A. Kwade, Intensive dry and wet mixing influencing the structural and electrochemical properties of secondary lithium-ion battery cathodes, *Electrochemical Society Transactions* 50 (26) (2013) 25–35.
- [2] G. Gaiselmann, M. Neumann, L. Holzer, T. Hocker, M. R. Prestat, V. Schmidt, Stochastic 3d modeling of  $\text{La}_{0.6}\text{Sr}_{0.4}\text{CoO}_{3-\delta}$  cathodes based on structural segmentation of fib–sem images, *Computational Materials Science* 67 (0) (2013) 48–62.
- [3] O. Stenzel, H. Hassfeld, R. Thiedmann, L. J. A. Koster, S. D. Oosterhout, S. S. van Bavel, M. M. Wienk, J. Loos, R. A. J. Janssen, V. Schmidt, Spatial modeling of the 3D morphology of hybrid polymer-ZnO solar cells, based on electron tomography data, *The Annals of Applied Statistics* 5 (3) (2011) 1920–1947.

- [4] A. Kwade, J. Schwedes, Breaking characteristics of different materials and their effect on stress intensity and stress number in stirred media mills, *Powder Technology* 122 (2) (2002) 109–121.
- [5] M. He, Y. Wang, E. Forsberg, Slurry rheology in wet ultrafine grinding of industrial minerals: a review, *Powder Technology* 147 (1) (2004) 94–112.
- [6] P. Richard, M. Nicodemi, R. Delannay, P. Ribiere, D. Bideau, Slow relaxation and compaction of granular systems, *Nature Materials* 4 (2) (2005) 121–128.
- [7] C. Schilde, T. Gothsch, K. Quarch, M. Kind, A. Kwade, Effect of important precipitation process parameters on the redispersion process and the micromechanical properties of precipitated silica, *Chemical Engineering & Technology* 32 (7) (2009) 1078–1087.
- [8] M. Doyle, T. F. Fuller, J. Newman, Modeling of galvanostatic charge and discharge of the lithium/polymer/insertion cell, *Journal of the Electrochemical Society* 140 (6) (1993) 1526–1533.
- [9] R. Grothausmann, G. Zehl, I. Manke, S. Fiechter, P. Bogdanoff, I. Dorbandt, A. Kupsch, A. Lange, M. P. Hentschel, G. Schumacher, Quantitative structural assessment of heterogeneous catalysts by electron tomography, *Journal of the American Chemical Society* 133 (45) (2011) 18161–18171.
- [10] P. A. Midgley, R. E. Dunin-Borkowski, Electron tomography and holography in materials science, *Nature Materials* 8 (4) (2009) 271–280.

- [11] H. Schulenburg, B. Schwanitz, N. Linse, G. G. Scherer, A. Wokaun, J. Krbanjevic, R. Grothausmann, I. Manke, 3D imaging of catalyst support corrosion in polymer electrolyte fuel cells, *The Journal of Physical Chemistry C* 115 (29) (2011) 14236–14243.
- [12] S. Zils, M. Timpel, T. Arlt, A. Wolz, I. Manke, C. Roth, 3D visualisation of PEMFC electrode structures using FIB nanotomography, *Fuel Cells* 10 (6) (2010) 966–972.
- [13] I. Manke, C. Hartnig, N. Kardjilov, H. Rieseemeier, J. Goebbels, R. Kuhn, P. Krüger, J. Banhart, In situ synchrotron X-ray radiography investigations of water transport in PEM fuel cells, *Fuel Cells* 10 (1) (2010) 26–34.
- [14] A. Haibel, I. Manke, A. Melzer, J. Banhart, In situ microtomographic monitoring of discharging processes in alkaline cells, *Journal of the Electrochemical Society* 157 (4) (2010) 387–391.
- [15] S. Strege, A. Weuster, H. Zetzener, L. Brendel, A. Kwade, D. Wolf, Approach to structural anisotropy in compacted cohesive powder, *Granular Matter* 16 (3) (2014) 401–409.
- [16] H. Markötter, I. Manke, R. Kuhn, T. Arlt, N. Kardjilov, M. P. Hentschel, A. Kupsch, A. Lange, C. Hartnig, J. Scholta, Neutron tomographic investigations of water distributions in polymer electrolyte membrane fuel cell stacks, *Journal of Power Sources* 219 (2012) 120–125.
- [17] G. B. Arfken, H. J. Weber, *Mathematical Methods for Physicists*, sixth edition, Elsevier Academic Press, Waltham, 2008.

- [18] E. W. Hobson, *The Theory of Spherical and Ellipsoidal Harmonics*, Chelsea Publishing Company, New York, 1955.
- [19] M. J. Mohlenkamp, A fast transform for spherical harmonics, *Journal of Fourier Analysis and Applications* 5 (2-3) (1999) 159–184.
- [20] B. Zhou, J. Wang, B. Zhao, Micromorphology characterization and reconstruction of sand particles using micro X-ray tomography and spherical harmonics, *Engineering Geology* 184 (2015) 126–137.
- [21] J. Ziegel, Stereological modelling of random particles, *Communications in Statistics-Theory and Methods* 42 (7) (2013) 1428–1442.
- [22] J. G. Calvert, Glossary of atmospheric chemistry terms (recommendations 1990), *Pure and Applied Chemistry* 62 (11) (1990) 2167–2219.
- [23] H. Wadell, Sphericity and roundness of rock particles, *The Journal of Geology* 41 (3) (1933) 310–331.
- [24] G. L. Samuel, M. S. Shunmugam, Evaluation of sphericity error from form data using computational geometric techniques, *International Journal of Machine Tools and Manufacture* 42 (3) (2002) 405–416.
- [25] A. M. Svane, Local digital algorithms for estimating the integrated mean curvature of r-regular sets, *Discrete & Computational Geometry* (submitted).
- [26] A. M. Svane, Estimation of intrinsic volumes from digital grey-scale images, *Journal of Mathematical Imaging and Vision* 49 (2) (2014) 352–376.

- [27] J. Ziegel, M. Kiderlen, Estimation of surface area and surface area measure of three-dimensional sets from digitizations, *Image and Vision Computing* 28 (1) (2010) 64–77.
- [28] J. W. Bullard, E. J. Garboczi, Defining shape measures for 3D star-shaped particles: Sphericity, roundness, and dimensions, *Powder Technology* 249 (2013) 241–252.
- [29] S. Tippmann, D. Walper, L. Balboa, B. Spier, W. G. Bessler, Low-temperature charging of lithium-ion cells - Part I: Electrochemical modeling and experimental investigation of degradation behavior, *Journal of Power Sources* 252 (2014) 305–316.
- [30] F. P. Preparata, M. I. Shamos (Eds.), *Computational Geometry: An Introduction*, Springer, New York, 1985.
- [31] R. Beare, G. Lehmann, The watershed transform in ITK - discussion and new developments, *The Insight Journal*.
- [32] S. Beucher, C. Lantuéjoul, Use of watersheds in contour detection, in: *Proceedings of the International workshop on image processing, real-time edge and motion detection/estimation*, Rennes, France, 1979.
- [33] S. Beucher, F. Meyer, The morphological approach to segmentation: the watershed transformation, in: E. Dougherty (Ed.), *Mathematical Morphology in Image Processing*, Marcel Dekker, New York, 1993, pp. 433–481.
- [34] J. Roerdink, A. Meijster, The watershed transform: definitions, al-

- gorithms, and parallelization strategies, *Fundamenta Informaticae* 41 (2001) 187–228.
- [35] S. Wilson, Training Structuring Elements in Morphological Networks, in: E. Dougherty (Ed.), *Mathematical Morphology in Image Processing*, Marcel Dekker, New York, 1993, pp. 1–42.
- [36] E. Garboczi, Three-dimensional mathematical analysis of particle shape using X-ray tomography and spherical harmonics: Application to aggregates used in concrete, *Cement and Concrete Research* 32 (10) (2002) 1621–1638.
- [37] C. van Loan, *Computational Frameworks for the Fast Fourier Transform*, *Frontiers in Applied Mathematics*, Society for Industrial and Applied Mathematics, Philadelphia, 1992.
- [38] G. Dahlquist, Å. Björck, *Numerical Methods in Scientific Computing: Volume 1*, SIAM e-books, Society for Industrial and Applied Mathematics, Philadelphia, 2008.
- [39] L. R. Rabiner, B. Gold, *Theory and Application of Digital Signal Processing*, Prentice-Hall, Englewood Cliffs, 1975.
- [40] G. Marsaglia, Choosing a point from the surface of a sphere, *The Annals of Mathematical Statistics* 43 (2) (1972) 645–646.
- [41] A. N. Kolmogorov, Sulla determinazione empirica di una legge di distribuzione, *Giornale dell’Istituto Italiano degli Attuari* 4 (1933) 83–91.
- [42] N. Smirnov, On the estimation of the discrepancy between empirical

- curves of distribution for two independent samples, *Moscow University Mathematics Bulletin* 2 (1939) 2–16.
- [43] L. Gaines, J. Sullivan, A. Burnham, I. Belharouak, Life-cycle analysis for lithium-ion battery production and recycling, in: *Transportation Research Board 90th Annual Meeting*, Washington, DC, 2011, pp. 23–27.
- [44] B. Scrosati, Recent advances in lithium ion battery materials, *Electrochimica Acta* 45 (15) (2000) 2461–2466.
- [45] H. Y. Tran, G. Greco, C. Täubert, M. Wohlfahrt-Mehrens, W. Haselrieder, A. Kwade, Influence of electrode preparation on the electrochemical performance of  $\text{LiNi}_{0.8}\text{Co}_{0.15}\text{Al}_{0.05}\text{O}_2$  composite electrodes for lithium-ion batteries, *Journal of Power Sources* 210 (2012) 276 – 285.
- [46] W. van Schalkwijk, B. Scrosati, *Advances in lithium-ion batteries*, Springer Science & Business Media, 2002.
- [47] S. Strege, H. Zetzener, A. Kwade, From particle to powder properties – a mesoscopic approach combining micro-scale experiments and X-ray microtomography, *AIP Conference Proceedings* 1542 (1) (2013) 839–842.
- [48] J. Angulo, D. Jeulin, Stochastic watershed segmentation, in: *Proceedings of the 8th International Symposium on Mathematical Morphology*, 2007, pp. 265–276.
- [49] M. Jourlin, I. Fillere, J.-M. Becker, M.-J. Labouré, Shapes and met-

- rics, in: *Computer Analysis of Images and Patterns*, Springer, 1993, pp. 254–258.
- [50] E. Parzen, On estimation of a probability density function and mode, *The Annals of Mathematical Statistics* 33 (3) (1962) 1065–1076.
- [51] M. Rosenblatt, Remarks on some nonparametric estimates of a density function, *The Annals of Mathematical Statistics* 27 (3) (1956) 832–837.
- [52] A. Baxansky, N. Kiryati, Calculating geometric properties of three-dimensional objects from the spherical harmonic representation, *Pattern Recognition* 40 (2) (2007) 756–770.
- [53] K. Schladitz, J. Ohser, W. Nagel, Measuring intrinsic volumes in digital 3D images, in: A. Kuba, L. G. Nyúl, K. Palágyi (Eds.), *Discrete Geometry for Computer Imagery*, Vol. 4245 of *Lecture Notes in Computer Science*, Springer, New York, 2006, pp. 247–258.
- [54] H. Wadell, Volume, shape and roundness of quartz particles, *The Journal of Geology* 43 (3) (1935) 250–280.
- [55] M. M. Kazhdan, T. A. Funkhouser, S. Rusinkiewicz, Rotation invariant spherical harmonic representation of 3D shape descriptors, in: *Proceedings of the 2003 Eurographics/ACM SIGGRAPH Symposium on Geometry Processing, SGP '03*, Eurographics Association, Aire-la-Ville, Switzerland, 2003, pp. 156–164.